ADVANCED FUNCTIONAL MATERIALS
www.afm-journal.de

Refining Energy Levels in ReS_2 Nanosheets by Low-Valent Transition-Metal Doping for Dual-Boosted Electrochemical Ammonia/Hydrogen Production

Feili Lai, Nan Chen, Xiaobin Ye, Guanjie He, Wei Zong, Katherine B. Holt, Bicai Pan, Ivan P. Parkin, Tianxi Liu, and Renjie Chen**

Electrocatalytic nitrogen reduction reaction (NRR) and hydrogen evolution reaction (HER) are intriguing approaches to nitrogen fixation and hydrogen production under ambient conditions, given the need to discover efficient and stable catalysts to light up the "green chemistry" future. However, bottlenecks are often found during N_2/H_2O activation, the very first step of NRR/HER, due to energetic electron injection from the surface of electrocatalysts. It is reported that the bottlenecks for both NRR and HER can be tackled by engineering the energy level via low-valent transition-metal doping, simultaneously, where rhenium disulfide (ReS_2) is employed as a model platform to prove the concept. The doped low-valent transition-metal domains (e.g., Fe, Co, Ni, Cu, Zn) in ReS_2 provide more active sites for N_2/H_2O chemisorption and electron transfer, not only weakening the N≡N/O−H bonds for easier dissociation through proton coupling, but also elevating *d*-band center toward the Fermi level with more electron energy for N_2/H_2O reduction. As a result, it is found that iron-doped ReS_2 nanosheets wrapped nitrogen-doped carbon nanofiber (Fe-ReS_2@N-CNF) catalyst exhibits superior electrochemical activity with eightfold higher ammonia production yield of 80.4 μg h^{-1} $mg^{-1}_{cat.}$, and lower onset overpotential of 146 mV and Tafel slope of 63 mV dec^{-1}, when comparing with the pristine ReS_2.

1. Introduction

Ammonia (NH_3) is an indispensable carbon-free chemical to agriculture and other products,[1–3] as well as a potential carrier for hydrogen storage due to its high hydrogen density and liquefiable feature.[4,5] However, the chemical inertness of dinitrogen (large bond energy of 940.95 kJ mol^{-1}),[6,7] makes it a "Cadmean victory" to convert N_2 into NH_3. For instance, the famous reaction for industrial ammonia production is known as Haber–Bosch process, relying on iron-based catalysts and rigorous operating conditions (673–873 K, 20–40 MPa),[8,9] which almost accounts for 1% of the worldwide energy consumption and 1.6% of the total global CO_2 emission.[10]

In order to promote the progress of "green chemistry", a clean, safe, and sustainable NH_3 synthesis route is an urgent need. Electrochemical nitrogen reduction reaction (NRR) has gradually attracted much attention, and been regarded as an alternative approach.[11–14] As an inevitably overwhelming rival, the hydrogen evolution reaction (HER) should be well impeded, making it a key issue to find a reasonable way to enhance N species adsorption on the surface of catalyst instead of H species. For instance, Ling et al. put forward a reticular chemistry approach by exploiting MOF's water-repelling and molecular-concentrated effects to overcome HER-imposed bottlenecks (MOF: metal–organic framework), achieving both excellent NRR selectivity (≈90%) and boosted Faradaic efficiency by 10 percentage points.[15] Recently, Yan et al. reported a strategy to simultaneously promote NRR selectivity and activity by using

Dr. F. Lai, W. Zong, Prof. T. Liu
The Key Laboratory of Synthetic and Biological Colloids
Ministry of Education
School of Chemical and Material Engineering
Jiangnan University
Wuxi 214122, P. R. China
E-mail: txliu@dhu.edu.cn
Dr. N. Chen, Prof. R. Chen
School of Materials Science & Engineering
Beijing Institute of Technology
Beijing 100081, P. R. China
E-mail: chenrj@bit.edu.cn
The ORCID identification number(s) for the author(s) of this article can be found under https://doi.org/10.1002/adfm.201907376.
X. Ye, Prof. B. Pan
Hefei National Laboratory for Physical Science at the Microscale
University of Science and Technology of China
Hefei, Anhui 230026, P. R. China
Dr. G. He, Prof. K. B. Holt, Prof. I. P. Parkin
Christopher Ingold Laboratory
Department of Chemistry
University College London
20 Gorden Street, London WC1H 0AJ, UK

DOI: 10.1002/adfm.201907376

bismuth nanocrystals and potassium cations, the Faradaic efficiency of which was achieved as 66%.[16] Yan et al. also proposed it can suppress the HER process and improve the Faradaic efficiency of NRR to 56.55% by positively shifting the reaction potential and using single-atom iron as electrocatalyst.[17] To our knowledge, however, traditional Haber–Bosch process will still be the main route for NH_3 production in the foreseeable future with a large amount usage of H_2 by steam reforming of fossil fuels, where HER would be a more attractive choice for renewable H_2 resources. In fact, the majority used hydrogen gas for Haber–Bosch process would go through a series of chemical treatment processes under high temperature, while less than 4% of the total H_2 gas comes from sustainable and mild electrocatalysis of water. Therefore, it would be also another possible perspective to explore dual-enhanced electrocatalysts for both ammonia and hydrogen production, as it is still difficult to suppress the HER process well for the majority electrocatalysts.

Bearing this in mind, rhenium disulfide (ReS_2) has been recently discovered as next-generation transition metal dichalcogenide (TMD) materials for high-efficient electrocatalysis.[18,19] It is mainly attributed to their layered structure with weak van der Waals interactions between individual sandwiched layers,[20,21] and anisotropic structure with two-dimensional (2D) morphology to provide not only large specific surface area but also 2D permeable channels for reactant adsorption/transport.[22] In the past few years, abundant effort has been made to promote the development of TMD-based electrocatalysts for both nitrogen reduction reaction and hydrogen evolution reaction.[23–25] In contrast with other TMD materials (such as MoS_2, $MoSe_2$, WS_2, and WSe_2), ReS_2 possesses a very weak interlayer coupling,[25–27] thus leading to an enhanced reactant diffusion into its deep interlayer space for better NRR/HER processes. Besides that, traces of transition-metal doping, particularly for low-valent domains (such as Fe^{3+}, Co^{2+}, Ni^{2+}, Cu^{2+}, Zn^{2+}),[28–30] in atomically ordered ReS_2 nanosheets can disturb its crystalline lattice to expose more active sites for electrocatalysis. However, several significant issues in low-valent transition-metal doped ReS_2 nanosheets are still rarely reported and urgently needed to be addressed and solved, namely, how does transition-metal incorporate into ReS_2, and where are the real electrocatalytic sites for NRR/HER?

Therefore, here we employ low-valent Fe^{3+}/Co^{2+}/Ni^{2+}/Cu^{2+}/Zn^{2+} salts deliberately for coprecipitation with ReO_4^- salt. By this, M^{4+}-positioned Re could be replaced by low-valent transition-metal species (e.g., Fe, Co, Ni, Cu, Zn). The density functional theory (DFT) calculation first reveals that the energy level of ReS_2 can be well tuned by doping engineering with enhanced charge density around the low-valent cations. Taking iron-doped ReS_2 nanosheets wrapped nitrogen-doped carbon nanofiber (Fe-ReS_2@N-CNF) catalyst as an example, it exhibits superior electrochemical activity with an eightfold higher ammonia production yield rate of 80.4 μg h^{-1} $mg^{-1}_{cat.}$ for NRR, and lower onset overpotential of 146 mV and Tafel slope of 63 mV dec^{-1} for HER, when comparing with the pristine ReS_2. The deep mechanisms for NRR/HER processes are further discovered by in situ spectroscopic characterization together with DFT studies that low-valent Fe domain is beneficial to providing more active sites for N_2/H_2O chemisorption and weakening the N≡N/O−H bonds for easier dissociation through proton coupling. These results clearly demonstrate the important role of low-valent transition-metal doping engineering on optimizing ReS_2-based NRR/HER electrocatalyst, which provides a novel but general route for green synthesis of NH_3 production.

2. Results and Discussion

Foreseen by computational study first, the pristine ReS_2 semiconductor shows a wide energy gap (E_g) of 1.31 eV (**Figure 1**a)

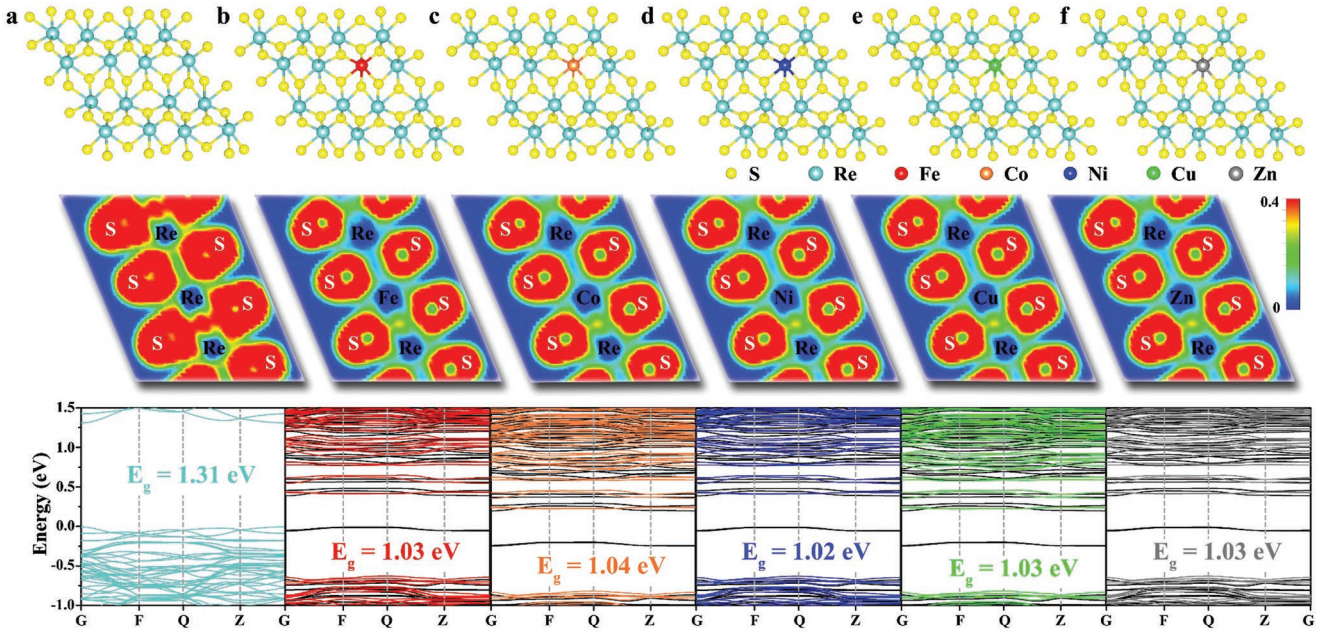

Figure 1. Atomistic models of crystal structure, two dimensional electron localization function (ELF) mappings, and calculated band structures for a) ReS_2, b) Fe-ReS_2, c) Co-ReS_2, d) Ni-ReS_2, e) Cu-ReS_2, and f) Zn-ReS_2, respectively.

as direct-band gap. This high E_g will certainly hinder the catalyst activation with inefficient electron transition. Interestingly, the other five kinds of optimized ReS_2 models were constructed by doping 5% low-valent transition-metals (e.g., Fe, Co, Ni, Co and Zn), denoted as Fe-ReS_2 (Figure 1b), Co-ReS_2 (Figure 1c), Ni-ReS_2 (Figure 1d), Cu-ReS_2 (Figure 1e), and Zn-ReS_2 (Figure 1f), respectively. As a result, we found the E_g values of these doped ReS_2 samples significantly decreased to around 1.03 eV as indirect-band gaps, demonstrating it a feasible strategy for superior electron excitation of transition-metal doped ReS_2. The well-reduced energy gap is attributed to the impurity band after doping of transition-metals, which can be either in the gap or in the valence/conduction band. Here, the first-principle calculations show that impurity band will live in the gap of transition-metal doped ReS_2, therefore the gap is decreased. Meanwhile, this may also be originated from the activate ReS_2 atomic surface with charge redistribution, especially centered around low-valance transition-metal doped domains (Figure 1 and Figure S1, Supporting Information),[31] which can be regarded as highly active electrocatalysts.

Inspired by the above theoretical results, iron-doped ReS_2 nanosheets wrapped nitrogen-doped carbon nanofiber (Fe-ReS_2@N-CNF) is first chosen as the key model system to investigate the benefits of low-valent transition-metal doping engineering. The samples are synthesized via an N-CNF templated hydrothermal method,[32] in which Fe atoms are doped into ReS_2 lattice using $FeCl_3 \cdot 6H_2O$ as a precursor as schematically illustrated in **Figure 2**a. First, the typical scanning electron microscopy (SEM) image of N-CNF is displayed in Figure 2b with average diameter of 30–60 nm, proving that the heteroatom doping process for nitrogen atoms would not affect its morphology (Figure S5, Supporting Information) and noncrystalline property (Figure S6, Supporting Information). The nitrogen-rich carbon surface is also beneficial to the adsorption of ReO_4^-/Fe^{3+} precursors for epitaxial growth of Fe-ReS_2 nanosheets. Figure 2c–e reveals the morphology of Fe-ReS_2@N-CNF by SEM and transmission electron microscopy (TEM), highlighting a feature of uniform Fe-ReS_2 nanosheets covered hybrid carbon nanofiber with ultrafine diameter of ≈85 nm and length extending to several micrometers. This hybrid strategy is beneficial to solving the difficult problem of Fe-ReS_2 aggregations (Figure S7, Supporting Information), leading to significantly increased specific surface area from 12.1 to 24.6 $cm^2\ g^{-1}$ (Figure S8, Supporting Information). As displayed in high-resolution TEM (HRTEM) image (Figure 2f), the iron-doped ReS_2 nanosheets with a spacing of 0.62 nm can be assigned to (001) planes, indicating that the Fe-ReS_2 mainly grow along [001] direction. Energy-dispersive X-ray spectroscopy (EDS) mapping is further employed to ascertain the doping of Fe and N elements on Fe-ReS_2@N-CNF-5, revealing the uniform Fe and N doping (Figure 2g). X-ray diffraction (XRD) exhibits the same Bragg reflections of Fe-ReS_2@N-CNF-5 and non-doped ReS_2@N-CNF (Figure 2h), implying no structural deformation caused by low-valent Fe substitution of Re^{4+}.

X-ray photoelectron spectroscopy (XPS) is further applied to understand the chemical states and elemental compositions in the Fe-ReS_2@N-CNF-5. The binding energies of the Re^{4+} $4f_{7/2}$ and $4f_{5/2}$ electron peaks in Fe-ReS_2@N-CNF-5 are 41.0 and 44.4 eV, respectively (**Figure 3**a).[33] As shown in Figure 3b, two characteristic peaks being located at 162.4 and 163.4 eV in Fe-ReS_2@N-CNF-5 are detected for the bonding configurations of S, corresponding to the core $2p_{3/2}$ and $2p_{1/2}$ level peaks of S^{2-}, respectively.[34] All these above results are consistent with values for ReS_2@N-CNF, indicating the immeasurable changes for chemical states of Re and S elements after doping iron atoms in Fe-ReS_2@N-CNF-5. Three types of pyridinic N (398.4 eV), pyrrolic N (400.3 eV), and graphitic N (401.1 eV) are identified from Fe-ReS_2@N-CNF-5 (Figure 3c), manifesting the successful incorporation of N atoms in the carbon nanofiber template. Meanwhile, the high pyridinic N content in Fe-ReS_2@N-CNF-5 can also promote the following ammonia production.[35] The binding energies of the Fe $2p_{3/2}$ and Fe $2p_{1/2}$ electron peaks in Fe-ReS_2@N-CNF-5 are 708.1 and 721.2 eV (Figure 3d), respectively, confirming the successful incorporation of Fe atoms in ReS_2 structure. In this instance, an obviously negative shift of binding energy for the Fe $2p_{3/2}$ electron is observed when compared with other iron compounds, such as binding energies of Fe $2p_{3/2}$ in Fe_2O_3 (710.1 eV), $FeCl_2$ (710.7 eV), and $FeCl_3$ (711.6 eV).[36] It can be ascribed to the bonding hybridization of Fe atom with its neighbor atoms, leading to the decreased oxidation state of Fe. After incorporating low-valent Fe element in ReS_2 nanosheets, the density distribution in Fe-ReS_2 is significantly destabilized to Fe-doped domains (*inset* in Figure 3d), due to the structural heterogeneity-leaded charge rearrangement. Furthermore, the quantitative analysis of XPS spectra (Figure S9, Supporting Information) demonstrates the chemical formula of 5 mol% Fe-doped ReS_2 nanosheets can be fixed to $Fe_{0.073}Re_{0.991}S_2$ (Table S1, Supporting Information).

Upon confirming the electronic structure of low-valent Fe doped ReS_2 compound, we are now in a position to evaluate the efficacy of as-obtained 5 mol% transition-metal doped ReS_2 nanosheets wrapped nitrogen-doped carbon nanofiber (Fe/Co/Ni/Cu/Zn-ReS_2@N-CNF-5) for electrochemical HER/NRR performance, which were tested under 0.1 M Na_2SO_4 solution with continuous N_2 bubbling. As shown in the polarization curves (**Figure 4**a) and Tafel plots (Figure 4b), the low-valent transition-metal doping could moderately improve the HER activity of non-doped ReS_2@N-CNF (Table S2, Supporting Information). Taking Fe-ReS_2@N-CNF as an example, it shows lower onset overpotential (η = 146 mV, the onset overpotential is defined as the difference between the reversible potential of the couple H_2/H^+ and the potential where electrocatalysis occurs) and Tafel slope (63 mV dec^{-1}) than those in ReS_2@N-CNF (η = 200 mV; 87 mV dec^{-1}), implying its superiority to accelerate the hydrogen evolution reaction by low-valent transition-metal doping engineering. As an efficient conductive-frame, nitrogen-doped carbon nanofiber is also beneficial for the electron transfer along the interface of N-CNF and ReS_2 outer layer, leading to the enhanced HER performance (Figure S12, Supporting Information). Fe-ReS_2@N-CNF-5 also shows remarkable durability (Figure S13, Supporting Information), without dramatic change of the LSV curve after 5000 cycles. Apart from positive effect of low-valent transition-metal doping engineering in HER activity, we also found it is useful in the improvement of NRR. As shown in Figure 4c, the maximum NH_3 yield rate (80.4 μg h^{-1} $mg^{-1}_{cat.}$) and Faradaic efficiency (FE = 12.3%) of Fe-ReS_2@N-CNF-5 are much higher than those of non-doped ReS_2@N-CNF (10.3 μg h^{-1} $mg^{-1}_{cat.}$,

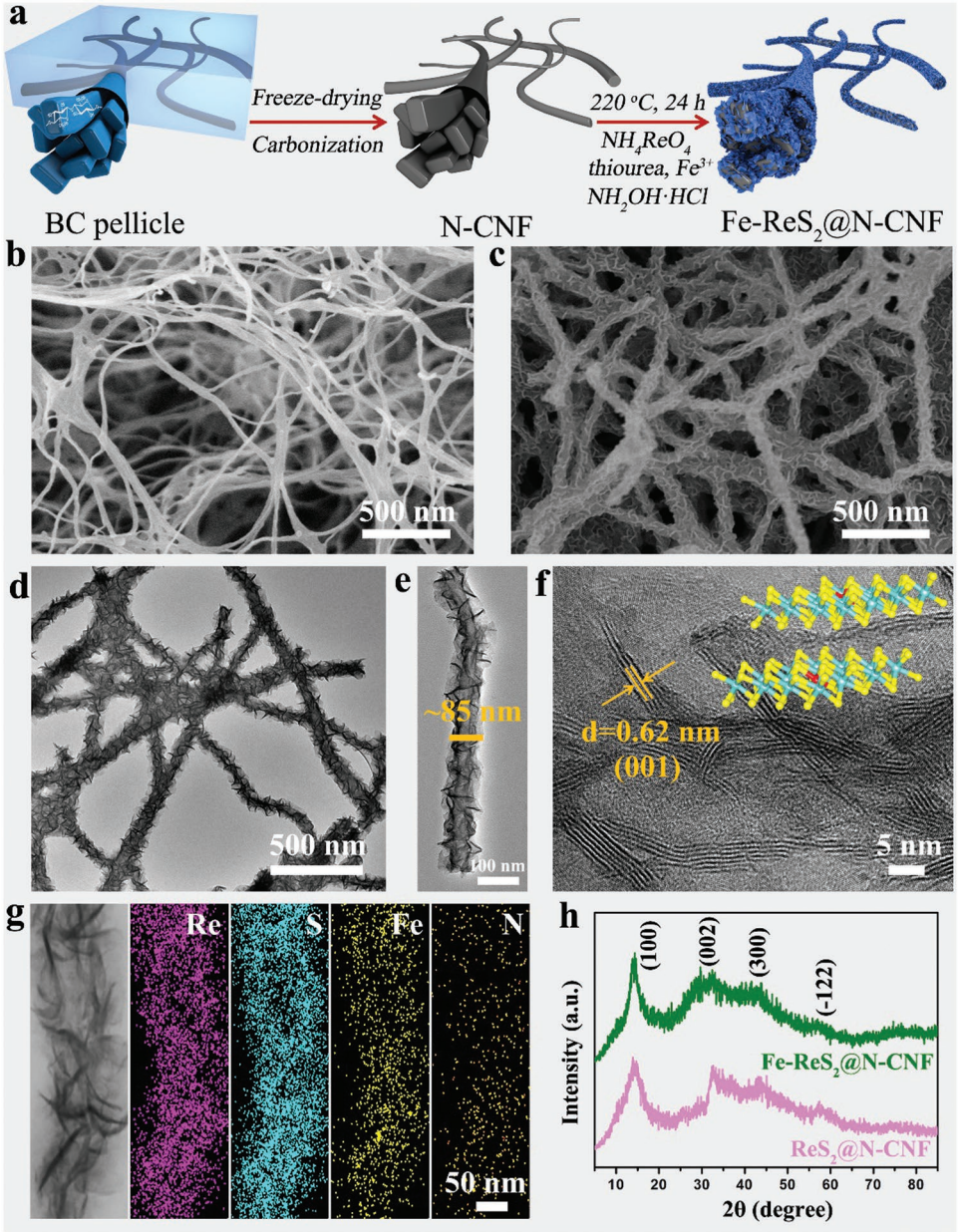

Figure 2. a) Schematic illustration of preparation process of Fe-ReS_2@N-CNF. SEM images of b) N-CNF and c) 5 mol % Fe-doped ReS_2@N-CNF (Fe-ReS_2@N-CNF-5). d,e) TEM images, f) HRTEM image, and g) corresponding element mapping of Fe-ReS_2@N-CNF-5. h) XRD patterns of Fe-ReS_2@N-CNF-5 and ReS_2@N-CNF.

FE = 9.9%) at -0.2 V versus reversible hydrogen electrode (RHE). In order to make the quantitative method for NH_3 yield rate more convincing, nuclear magnetic resonance (NMR) method was further applied (Figure S20a, Supporting Information). Based on the corresponding fitted curve (Figure S20b, Supporting Information), the NH_3 yield rate can be calculated to be 79.8 μg h^{-1} $mg^{-1}_{cat.}$, which approached to the NH_3 yield rate from indophenol blue method within the allowed error range, demonstrating the reliability of detection methods (NMR and indophenol blue methods). This enhanced NRR performance can also be observed in other low-valent transition-metal doped electrodes of Co/Ni/Cu/Zn-ReS_2@N-CNF-5 (Figure S21 and Table S3, Supporting Information). To verify the source of ammonia production, NMR method was conducted as ^{15}N isotopic labeling experiments. As displayed in Figure S22, Supporting Information, only ^{14}N triplets and ^{15}N doublets were observed in the $^{14}NH_4^+$ and $^{15}NH_4^+$ productions, respectively, by using $^{14}N_2$ and $^{15}N_2$ as feeding gases, which demonstrate not only the purity of as-used $^{14}N_2$ gas but also the stable structure of Fe-ReS_2@N-CNF-5 electrocatalyst without escaped N atoms during NRR process. Meanwhile, it was revealed that the Fe-doping concentrations would be closely related with the corresponding NRR performance (especially for NH_3 yield), 5% Fe-doping amount would be a more proper concentration

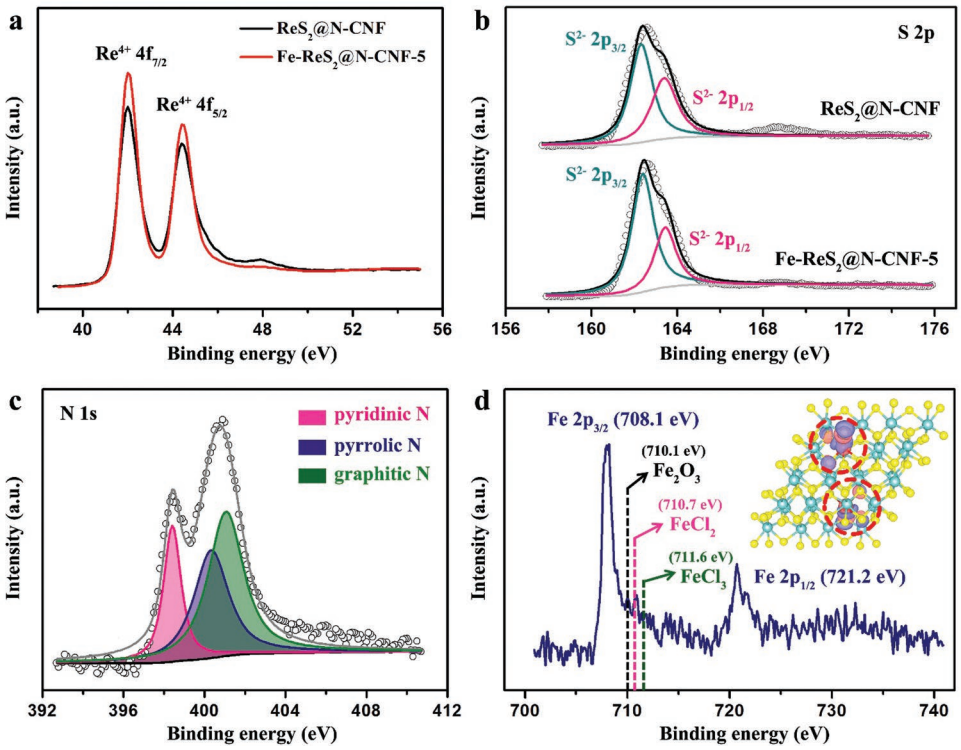

Figure 3. High-resolution XPS spectra of a) Re 4*f* and b) S 2*p* peaks for Fe-ReS_2@N-CNF-5 and ReS_2@N-CNF, respectively. High-resolution XPS spectra of c) N 1*s* and d) Fe 2*p* for Fe-ReS_2@N-CNF-5.

to release the best electrocatalytic activity for Fe-ReS_2 samples (Figure S24, Supporting Information). Both the NH_3 yield rates and FE_{NH3} values for Fe-ReS_2@N-CNF-5 are also well maintained with a stability retaining of ≈99% after ten continuous electrochemical NRR tests (Figure 4d). From the corresponding XPS spectra (Figure S25, Supporting Information), the Fe-ReS_2@N-CNF-5 still maintains the same chemical states and elemental compositions after NRR stability test as the ones before electrocatalysis (Figure 3), demonstrating its excellent electrocatalytic stability for long-term usage. As shown in Figure S26, Supporting Information, the sum of the amounts for generated NH_3 production (S2) and H_2 production (S1) equals the total supplied charge amount (S1 + S3), which indicates all the supplied charge was used to reduce neither N_2 gas nor H_2O molecules with a Faradaic efficiency of 87.7% for HER process. The rough agreement of the charge amount (S2 ≈ S3) between experimentally quantified gases (NH_3 and H_2) and calculated one suggests the total FE is 100% for the sum of NRR and HER without hydrazine generation (Figure S28, Supporting Information).

These enhanced NRR and HER performances in Fe-ReS_2@N-CNF-5 can be attributed to the refined energy levels of ReS_2 nanosheets after low-valent transition-metal doping, as predicted by DFT calculations in Figure 1. Experimentally, ultraviolet photoelectron spectroscopy (UPS) was used to determine the values of energy level (difference between the vacuum and Fermi level) of Fe-ReS_2 and pure ReS_2 as 6.11 and 7.27 eV (Figure 4e and Figure S29, Supporting Information), respectively, by subtracting the width of the He I UPS spectra at excitation energy of 21.22 eV. Compared with the energy level of non-doped ReS_2 nanosheets, the one of Fe-ReS_2 is properly shifted to approach the reduction potentials of H_2O and N_2 (Figure 4f), making the electron exchange process (Figure S30, Supporting Information) easier between electrocatalyst and the reacting species.[30] Due to the increased energy levels of Fe-ReS_2 nanosheets, the energy required for electron removal from the catalyst surface decreases, leading to the thermodynamically activated NRR and HER. In another perspective, the feasibility of electron transfer in low-valent transition-metal doped ReS_2 electrocatalysts would deliver lower onset overpotentials, demonstrating Fe-ReS_2@N-CNF-5 as a promising electrocatalyst for NRR and HER processes. Additionally, the incorporation of highly conductive N-CNF template is beneficial to increasing the electron transfer between two components in the Fe-ReS_2@N-CNF-5 for efficient reduction reaction as compared with that in Fe-ReS_2 bulk (Figure S31, Supporting Information).

Apart from the perspective of thermodynamics, kinetics also plays a key role in these reactions. Attributing to N-CNF template and low-valance Fe doping, Fe-ReS_2@N-CNF-5 displays an increased number of electroactive sites (evidenced by the N_2 adsorption-desorption isotherms in Figure S8, Supporting Information, and optimized electronic structure in Figure 3d), leading to the optimal activation effect of H_3O^+ and N_2 reagents on catalyst surface. For the HER process (**Figure 5**a), the H_3O^+ molecule interacts between $Re^{\delta+}/Fe^{\delta+}\cdots O$ and $S^{\delta-}\cdots H$ synergistically, as the first volmer step ($H_2O + e^- \rightarrow H_{ads} + OH^-$). After the adsorption of another H_2O molecule, the H_2 gas generates by following one kind of desorption steps ($H_{ads} + H_2O + e^- \rightarrow H_2 + OH^-$ or $H_{ads} + H_{ads} \rightarrow H_2$). As revealed by DFT calculation further (Figure S32, Supporting Information), the free

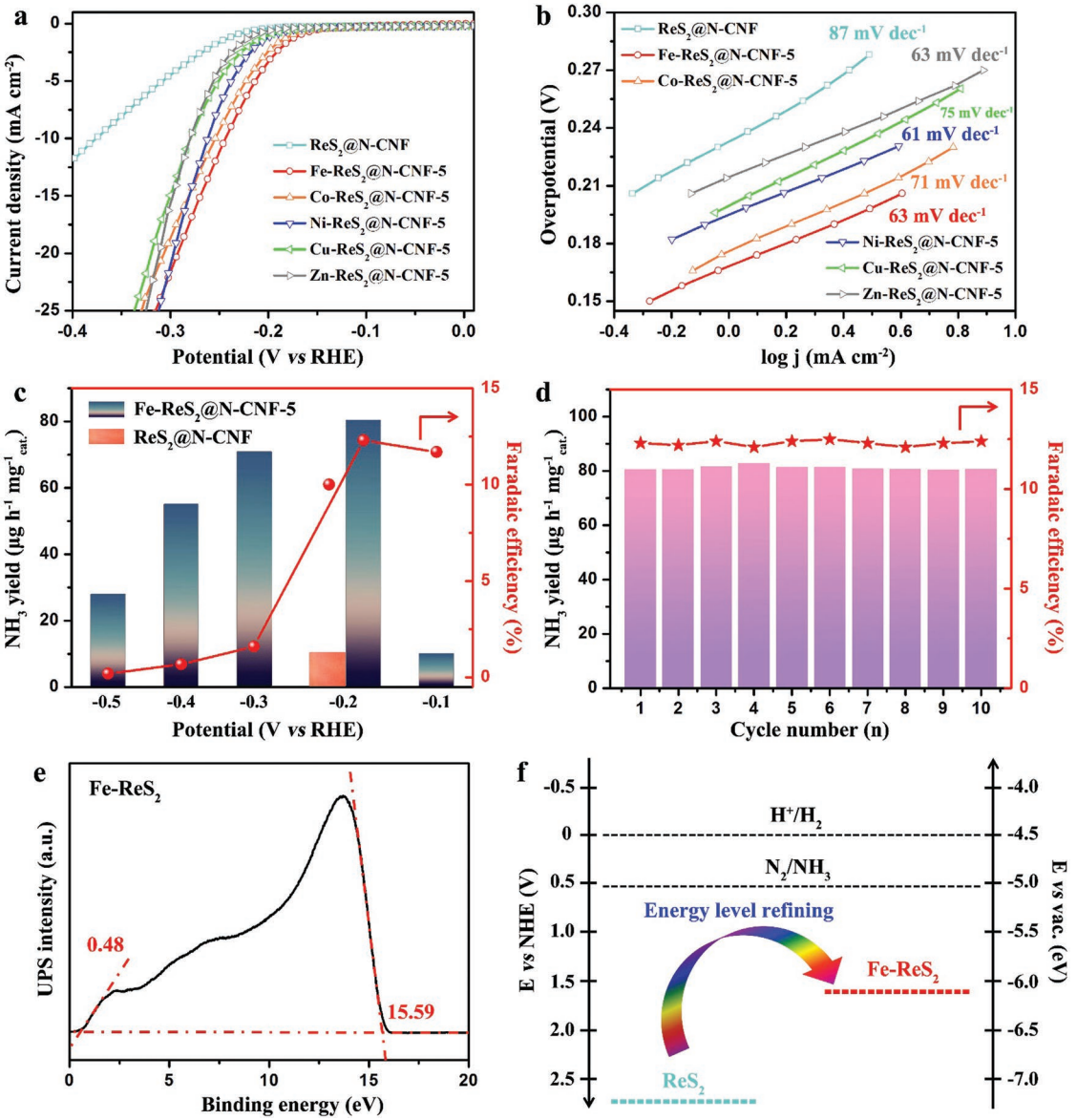

Figure 4. Electrocatalytic HER/NRR of 5 mol% transition-metal-doped ReS_2 nanosheets wrapped nitrogen-doped carbon nanofiber (Fe/Co/Ni/Cu/Zn-ReS_2@N-CNF-5) and non-doped ReS_2@N-CNF catalysts in aqueous solution of 0.1 M Na_2SO_4 under ambient conditions. a) Polarization curves. b) Tafel curves. c) The NH_3 production rates (bar graph) and FE_{NH3} (red line) of Fe-ReS_2@N-CNF-5 and ReS_2@N-CNF at different potentials. d) NRR stability test of Fe-ReS_2@N-CNF-5 at –0.2 V versus RHE. e) UPS spectra of Fe-ReS_2 nanosheets. f) Band structure diagram for Fe-ReS_2 and pure ReS_2.

energy value for H* (where * denotes as an adsorption site) is –0.36 eV for the pure ReS_2, but the water adsorption energy is up to 0.81 eV, which lead to the sluggish HER kinetics. Although the free energy value for H* in Fe-ReS_2 is relatively higher to be –0.49 eV, its water adsorption energy can be drastically reduced to 0.29 eV, indicating it is thermodynamically favorable for water reduction on Fe-ReS_2 in neutral solution. To further investigate the nitrogen reduction reaction process (Figure 5a), in situ attenuated total reflectance infrared (ATR IR) spectroscopy measurements were carried out for Fe-ReS_2@N-CNF-5 sample (Figure 5b–d). The IR bands at about 3420 and 1646 cm^{-1} (Figure 5b) match well with the O—H stretching and H—O—H bending of water molecules, respectively. Their positive shift with the decrease of applied potential from 0 to –0.3 V is attributed to the change of the adsorption configuration of water.[37] The peaks at 1554/1519, 1330 and 1102 cm^{-2} are attributed to the H—N—H bending,[38,39] —NH_2 wagging,[13,40] and N—N stretching[41,42] of adsorbed N_2H_y species, respectively. These results demonstrate that the nitrogen reduction reaction on Fe-ReS_2 follows an associative mechanism, instead of dissociative mechanism in the Haber-Bosch process,[43] with the simultaneous addition of hydrogen on N_2 to break the N≡N bond. The time-dependent SEIRAS spectra (Figure 5d) of Fe-ReS_2@N-CNF-5 catalyst at –0.2 V show similar absorption results with time goes, demonstrating its ultra-stable electrocatalysis. As reported in previous literature, enzymatic mechanism

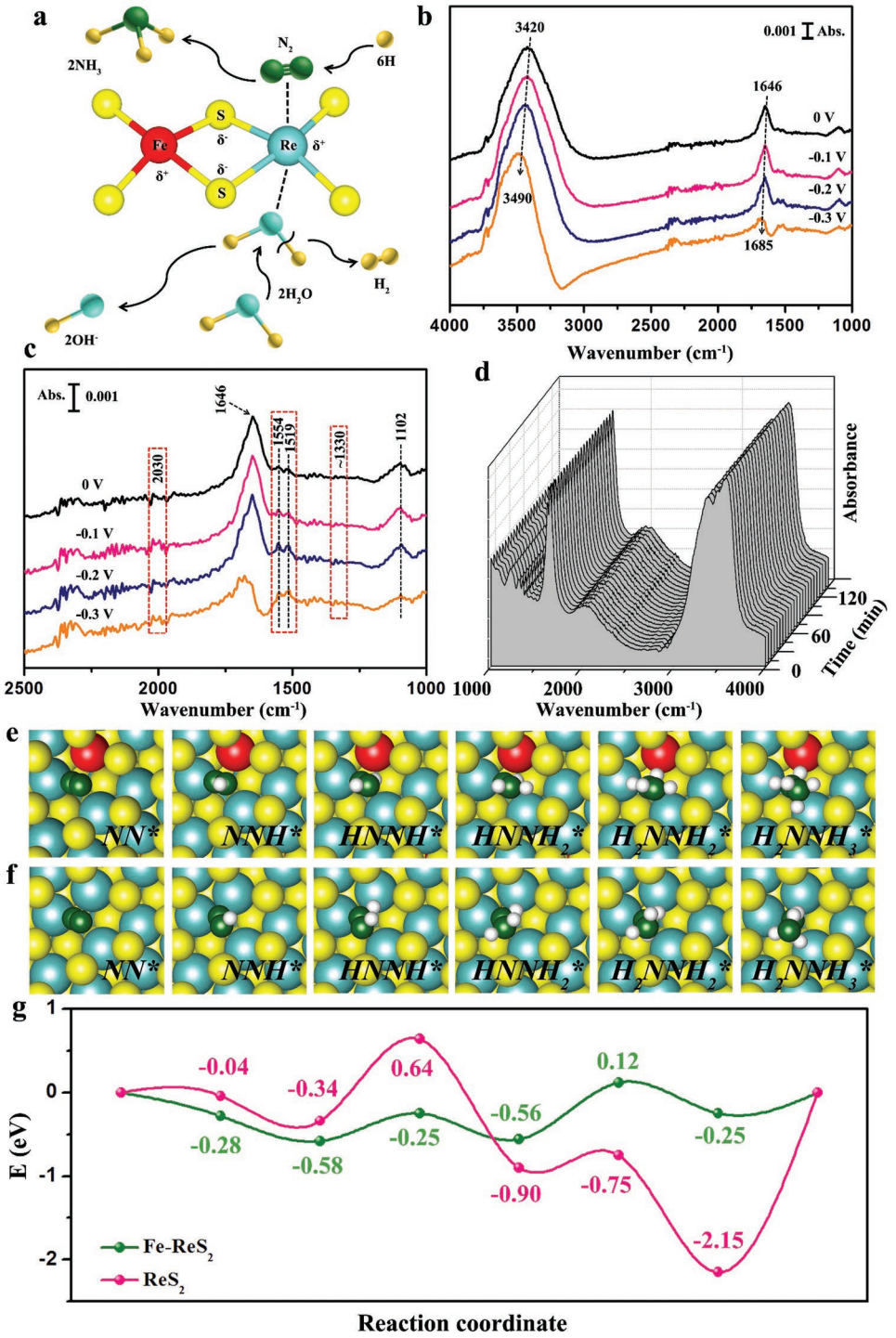

Figure 5. a) The proposed mechanism on uncoordinated Fe (δ^+) and Re (δ^+) centers during NRR and HER processes. b) In situ ATR IR spectra from 0 to –0.3 V on the Fe-ReS_2@N-CNF-5 catalyst in an N_2-saturated 0.1 M Na_2SO_4 solution. c) Amplification of the selected area in (b). d) Time-dependent ATR IR spectra of Fe-ReS_2@N-CNF-5 catalyst at a voltage of –0.2 V. Optimized structures of NH*, NNH*, HNNH*, $HNNH_2$*, H_2NNH_2*, and H_2NNH_3 intermediates on: e) Fe-ReS_2 and f) ReS_2. g) Free energy diagram of NRR on Fe-ReS_2 and ReS_2.

of N_2 fixation is more suitable for single-atom-embedded systems with lower energy barrier.[44,45] Therefore, the possible NRR mechanism is depicted in Figure S33, Supporting Information, with DFT calculation results in Figure 5e–g. All the reaction intermediates were bounded simultaneously to the surface Re atoms of both Fe-ReS_2 and ReS_2, while the Re atoms neighboring Fe atom showed higher activity for the reactions of N-related species (Figures 5e,f). The calculation results further

indicate the active sites in Fe-ReS_2 are located in the region near doped Fe atoms (especially for the Re atoms), which is corresponded with the ELF mappings (Figure 1) and destabilized density distribution (inset in Figure 3d). Further revealed by the free energy diagram (Figure 4g), the adsorption energy of nitrogen on Fe-ReS_2 (–0.28 eV) is much smaller than that on ReS_2 (–0.04 eV), which demonstrates that nitrogen is preferred to be adsorbed and activated on the Fe-doped surface of Fe-ReS_2. Subsequently, six consecutive protonation and reduction processes were canvassed as N_2 (g)* → NNH* → HNNH* → $HNNH_2$* → H_2NNH_2* → NH_2* + NH_3 → NH_3 (Table S4, Supporting Information). For the reaction pathway on ReS_2, the NH_3 desorption step is the rate-determining step during NRR process due to the highest energy barrier demand of 2.15 eV; While the transformation of $HNNH_2$* → H_2NNH_2* becomes the rate-determining step for the reaction pathway on Fe-ReS_2 with a relatively lower energy barrier demand of 0.68 eV. The results indicate that the Fe-doped surface of Fe-ReS_2 is beneficial to providing more active sites for highly kinetic NRR process.

3. Conclusions

In summary, we demonstrate that modulating the energy level of electrocatalysts by low-valent transition-metal doping engineering is an effective strategy to improve the NRR and HER activity of ReS_2 based catalysts. By means of electrochemical analysis, in situ ATR IR, and DFT studies, we show the introduction of low-valent Fe motifs into ReS_2 structures results in the formation of abundant anchor sites for direct adsorption and subsequent activation of N_2 molecules, which are responsible for the significantly improved NRR and HER intrinsic activities. Our work unravels the important role of low-valent transition-metal on energy level refining for electrocatalysis optimization, which may also be used in many other catalytic systems.

Supporting Information

Supporting Information is available from the Wiley Online Library or from the author.

Acknowledgements

This work was financially supported by the National Natural Science Foundation of China (51433001, 21674019, 21604010, 51671003, 21802003), the China Postdoctoral Science Foundation (2016M600268, 2017T100255, 2017M620494, 2018M631239), the Program of Shanghai Academic Research Leader (17XD1400100), the National Key Research and Development Program of China (Grant No. 2016YFB0100201), and the "Chenguang Program" supported by the Shanghai Education Development Foundation and Shanghai Municipal Education Commission. The computational center of USTC is acknowledged for computational support.

Conflict of Interest

The authors declare no conflict of interest.

Keywords

electrocatalysis, nitrogen reduction reaction, rhenium disulfide, transition-metals

Received: September 5, 2019
Revised: December 3, 2019
Published online:

[1] R. Raja, G. Sankar, J. M. Thomas, *J. Am. Chem. Soc.* **2001**, *123*, 8153.
[2] J. W. Erisman, M. A. Sutton, J. Galloway, Z. Klimont, W. Winiwarter, *Nat. Geosci.* **2008**, *1*, 636.
[3] M. A. Legare, G. Belanger-Chabot, R. D. Dewhurst, E. Welz, I. Krummenacher, B. Engels, H. Braunschweig, *Science* **2018**, *359*, 896.
[4] R. Lan, J. Irvine, S. W. Tao, *Int. J. Hydrogen Energy* **2012**, *37*, 1482.
[5] A. Klerke, C. H. Christensen, J. K. Norskov, T. Vegge, *J. Mater. Chem.* **2008**, *18*, 2304.
[6] D. Bao, Q. Zhang, F. L. Meng, H. X. Zhong, M. M. Shi, Y. Zhang, J. M. Yan, Q. Jiang, X. B. Zhang, *Adv. Mater.* **2017**, *29*, 16047993.
[7] N. Zhang, A. Jalil, D. X. Wu, S. M. Chen, Y. F. Liu, C. Gao, W. Ye, Z. M. Qi, H. X. Ju, C. M. Wang, X. J. Wu, L. Song, J. F. Zhu, Y. J. Xiong, *J. Am. Chem. Soc.* **2018**, *140*, 9434.
[8] A. Banerjee, B. D. Yuhas, E. A. Margulies, Y. B. Zhang, Y. Shim, M. R. Wasielewski, M. G. Kanatzidis, *J. Am. Chem. Soc.* **2015**, *137*, 2030.
[9] S. Licht, B. C. Cui, B. H. Wang, F. F. Li, J. Lau, S. Z. Liu, *Science* **2014**, *345*, 637.
[10] C. van der Ham, M. Koper, D. Hetterscheid, *Chem. Soc. Rev.* **2014**, *43*, 5183.
[11] C. X. Guo, J. R. Ran, A. Vasileff, S. Z. Qiao, *Energy Environ. Sci.* **2018**, *11*, 45.
[12] V. Kyriakou, I. Garagounis, E. Vasileiou, A. Vourros, M. Stoukides, *Catal. Today* **2017**, *286*, 2.
[13] Y. Yao, S. Q. Zhu, H. J. Wang, H. Li, M. H. Shao, *J. Am. Chem. Soc.* **2018**, *140*, 1496.
[14] C. Lv, Y. M. Qian, C. S. Yan, Y. Ding, Y. Y. Liu, G. Chen, G. H. Yu, *Angew. Chem., Int. Ed.* **2018**, *57*, 10246; *Angew. Chem.* **2018**, *130*, 10403.
[15] H. K. Lee, C. Koh, Y. H. Lee, C. Liu, I. Y. Phang, X. M. Han, C. K. Tsung, X. Y. Ling, *Sci. Adv.* **2018**, *4*, eaar3208.
[16] Y. C. Hao, Y. Guo, L. W. Chen, M. Shu, X. Y. Wang, T. A. Bu, W. Y. Gao, N. Zhang, X. Su, X. Feng, J. W. Zhou, C. W. Hu, A. X. Yin, R. Si, Y. W. Zhang, C. H. Yan, *Nat. Catal.* **2019**, *2*, 448.
[17] M. F. Wang, S. S. Liu, T. Qian, J. Liu, J. Q. Zhou, H. Q. Ji, J. Xiong, J. Zhong, C. L. Yan, *Nat. Commun.* **2019**, *10*, 341.
[18] F. Qi, X. Q. Wang, B. J. Zheng, Y. F. Chen, B. Yu, J. H. Zhou, J. R. He, P. J. Li, W. L. Zhang, Y. R. Li, *Electrochim. Acta* **2017**, *224*, 593.
[19] J. Gao, L. Li, J. W. Tan, H. Sun, B. C. Li, J. C. Idrobo, C. V. Singh, T. M. Lu, N. Koratkar, *Nano Lett.* **2016**, *16*, 3780.
[20] X. Huang, Z. Zeng, H. Zhang, *Chem. Soc. Rev.* **2013**, *42*, 1934.
[21] J. F. Xie, J. J. Zhang, S. Li, F. Grote, X. D. Zhang, H. Zhang, R. X. Wang, Y. Lei, B. C. Pan, Y. Xie, *J. Am. Chem. Soc.* **2013**, *135*, 17881.
[22] X. D. Zhang, Y. Xie, *Chem. Soc. Rev.* **2013**, *42*, 8187.
[23] L. Zhang, X. Q. Ji, X. Ren, Y. J. Ma, X. F. Shi, Z. Q. Tian, A. M. Asiri, L. Chen, B. Tang, X. P. Sun, *Adv. Mater.* **2018**, *30*, 1800191.
[24] X. D. Li, T. S. Li, Y. J. Ma, Q. Wei, W. B. Qiu, H. R. Guo, X. F. Shi, P. Zhang, A. M. Asiri, L. Chen, B. Tang, X. P. Sun, *Adv. Energy Mater.* **2018**, *8*, 1801357.
[25] Q. Zhang, S. J. Tan, R. G. Mendes, Z. T. Sun, Y. T. Chen, X. Kong, Y. H. Xue, M. H. Rummeli, X. J. Wu, S. L. Chen, L. Fu, *Adv. Mater.* **2016**, *28*, 2616.

[26] S. Tongay, H. Sahin, C. Ko, A. Luce, W. Fan, K. Liu, J. Zhou, Y. S. Huang, C. H. Ho, J. Y. Yan, D. F. Ogletree, S. Aloni, J. Ji, S. S. Li, J. B. Li, F. M. Peeters, J. Q. Wu, *Nat. Commun.* **2014**, *5*, 3252.
[27] S. Horzum, D. Cakir, J. Suh, S. Tongay, Y. S. Huang, C. H. Ho, J. Wu, H. Sahin, F. M. Peeters, *Phys. Rev. B* **2014**, *89*, 15543315.
[28] Z. Cai, D. J. Zhou, M. Y. Wang, S. M. Bak, Y. S. Wu, Z. S. Wu, Y. Tian, X. Y. Xiong, Y. P. Li, W. Liu, S. Siahrostami, Y. Kuang, X. Q. Yang, H. H. Duan, Z. X. Feng, H. L. Wang, X. M. Sun, *Angew. Chem., Int. Ed.* **2018**, *57*, 9392; *Angew. Chem.* **2018**, *130*, 9536.
[29] S. H. Ye, Z. X. Shi, J. X. Feng, Y. X. Tong, G. R. Li, *Angew. Chem., Int. Ed.* **2018**, *57*, 2672; *Angew. Chem.* **2018**, *130*, 2702.
[30] Y. Shi, Y. Zhou, D. R. Yang, W. X. Xu, C. Wang, F. B. Wang, J. J. Xu, X. H. Xia, H. Y. Chen, *J. Am. Chem. Soc.* **2017**, *139*, 15479.
[31] F. L. Lai, J. R. Feng, X. B. Ye, W. Zong, G. J. He, Y. E. Miao, X. M. Han, X. Y. Ling, I. P. Parkin, B. C. Pan, Y. F. Sun, T. X. Liu, *J. Mater. Chem. A* **2019**, *7*, 827.
[32] F. L. Lai, D. Y. Yong, X. L. Ning, B. C. Pan, Y. E. Miao, T. X. Liu, *Small* **2017**, *13*, 1602866.
[33] C. M. Corbett, C. Mcclellan, A. Rai, S. S. Sonde, E. Tutuc, S. K. Banerjee, *ACS Nano* **2015**, *9*, 363.
[34] J. Gao, L. Li, J. W. Tan, H. Sun, B. C. Li, J. C. Idrobo, C. V. Singh, T. M. Lu, N. Koratkar, *Nano Lett.* **2016**, *16*, 3780.
[35] Y. Liu, Y. Su, X. Quan, X. F. Fan, S. Chen, H. T. Yu, H. M. Zhao, Y. B. Zhang, J. J. Zhao, *ACS Catal.* **2018**, *8*, 1186.
[36] A. P. Grosvenor, B. A. Kobe, M. C. Biesinger, N. S. McIntyre, *Surf. Interface Anal.* **2004**, *36*, 1564.
[37] K. Ataka, T. Yotsuyanagi, M. Osawa, *J. Phys. Chem.* **1996**, *100*, 10664.
[38] S. D. Lin, A. C. Gluhoi, B. E. Nieuwenhuys, *Catal. Today* **2004**, *90*, 3.
[39] L. K. Xu, Y. L. Xin, J. T. Wang, *Electrochim. Acta* **2009**, *54*, 1820.
[40] G. Ramis, L. Yi, G. Busca, M. Turco, E. Kotur, R. J. Willey, *J. Catal.* **1995**, *157*, 523.
[41] Y. Ikezawa, T. Sawatari, T. Kitazume, H. Goto, K. Toriba, *Electrochim. Acta* **1998**, *43*, 3297.
[42] W. Gulaczyk, M. Kreglewski, A. Valentin, *J. Mol. Spectrosc.* **2003**, *220*, 132.
[43] J. H. Montoya, C. Tsai, A. Vojvodic, J. K. Norskov, *ChemSusChem* **2015**, *8*, 2180.
[44] X. Ma, J. Liu, H. Xiao, H. Li, M. H. Shao, *J. Am. Chem. Soc.* **2018**, *140*, 46.
[45] J. X. Zhao, Z. F. Chen, *J. Am. Chem. Soc.* **2017**, *139*, 12480.

